



Publication Year	2018
Acceptance in OA	2020-10-13T16:10:09Z
Title	The performance of the ATHENA X-ray Integral Field Unit
Authors	Peille, Philippe, den Hartog, Roland, MACCULI, CLAUDIO, Barbera, Marco, LOTTI, Simone, Cucchetti, Edoardo, Kirsch, Christian, Dauser, Thomas, Wilms, Joern, Bandler, Simon R., Smith, Stephen J., Jackson, Brian, Geoffray, Hervé, Mesnager, Jean-Michel, Pajot, François, Barret, Didier, Lam-Trong, Thien, den Herder, Jan-Willem, PIRO, LUIGI
Publisher's version (DOI)	10.1117/12.2313720
Handle	http://hdl.handle.net/20.500.12386/27783
Serie	PROCEEDINGS OF SPIE
Volume	10699

PROCEEDINGS OF SPIE

[SPIDigitalLibrary.org/conference-proceedings-of-spie](https://spiedigitallibrary.org/conference-proceedings-of-spie)

The performance of the ATHENA X-ray Integral Field Unit

Peille, Philippe, den Hartog, Roland, Macculi, Claudio, Barbera, Marco, Lotti, Simone, et al.

Philippe Peille, Roland den Hartog, Claudio Macculi, Marco Barbera, Simone Lotti, Edoardo Cucchetti, Christian Kirsch, Thomas Dauser, Joern Wilms, Simon R. Bandler, Stephen J. Smith, Brian Jackson, Hervé Geoffray, Jean-Michel Mesnager, François Pajot, Didier Barret, Thien Lam-Trong, Jan-Willem den Herder, Luigi Piro, "The performance of the ATHENA X-ray Integral Field Unit," Proc. SPIE 10699, Space Telescopes and Instrumentation 2018: Ultraviolet to Gamma Ray, 106994K (6 July 2018); doi: 10.1117/12.2313720

SPIE.

Event: SPIE Astronomical Telescopes + Instrumentation, 2018, Austin, Texas, United States

The performance of the Athena X-ray Integral Field Unit

Philippe Peille^a, Roland den Hartog^b, Claudio Macculi^c, Marco Barbera^d, Simone Lotti^c, Edoardo Cucchetti^e, Christian Kirsch^f, Thomas Dauser^f, Joern Wilms^f, Simon R. Bandler^g, Stephen J. Smith^g, Brian Jackson^b, Hervé Geoffroy^a, Jean-Michel Mesnager^a, François Pajot^e, Didier Barret^e, Thien Lam-Trong^a, Jan-Willem den Herder^b, and Luigi Piro^c

^aCentre National d'Etudes Spatiales, Centre spatial de Toulouse, 18 avenue Edouard Belin, 31401 Toulouse Cedex 9, France

^bSRON, Netherlands Institute for Space Research, Sorbonnelaan 2, 3584 CA Utrecht
^cINAF/Istituto di Astrofisica e Planetologia Spaziali, Via Fosso del Cavaliere 100, 00133, Roma, Italy

^dUniversità degli Studi di Palermo, Dipartimento di Fisica e Chimica, Via Archira 36, 90123 Palermo, Italy and INAF/Osservatorio Astronomico di Palermo G.S. Vaiana, Piazza del Parlamento 1, 90134 Palermo, Italy

^eInstitut de Recherche en Astrophysique et Planétologie, Université de Toulouse, CNRS, UPS, CNES, 9 Av. colonel Roche, BP 44346, F-31028 Toulouse Cedex 4, France

^fECAP, University of Erlangen-Nuremberg Sternwartstr. 7 96049 Bamberg, Germany

^gNASA/Goddard Space Flight Center, 8800 Greenbelt Rd, Greenbelt, MD 20771, United States

ABSTRACT

The X-ray Integral Field Unit (X-IFU) is a next generation microcalorimeter planned for launch onboard the Athena observatory. Operating a matrix of 3840 superconducting Transition Edge Sensors at 90 mK, it will provide unprecedented spectro-imaging capabilities (2.5 eV resolution, for a field of view of 5') in the soft X-ray band (0.2 up to 12 keV), enabling breakthrough science. The definition of the instrument evolved along the phase A study and we present here an overview of its predicted performances and their modeling, illustrating how the design of the X-IFU meets its top-level scientific requirements. This article notably covers the energy resolution, count-rate capability, quantum efficiency and non X-ray background levels, highlighting their main drivers.

Keywords: Athena, X-ray Integral Field Unit, X-rays, microcalorimeter, performances

1. INTRODUCTION

Scheduled for launch in the early 2030s on board the *Athena* X-ray observatory, the X-ray Integral Field Unit (X-IFU) [1] will enable breakthrough observations for a large variety of astrophysical objects, from the most distant and faintest galaxy clusters, to the brightest galactic X-ray binaries. With its energy resolution of 2.5 eV (FWHM) at 7 keV, it will indeed provide unprecedented spectro-imaging capabilities in the soft X-ray band (0.2 up to 12 keV) across a field of view of 5' equivalent diameter with a 5" pixel resolution. To do so, this instrument will operate a matrix of 3840 Transition Edge Sensors (TES) at 90 mK [2], voltage biased in their transition between the superconducting and normal states, and read out using a Frequency Domain Multiplexing scheme (FDM) with a multiplexing factor of 40 [3–5]. The TESs will be operated as microcalorimeters: the heat generated by a photon impact will induce a rapid change in their resistance, creating a current pulse whose shape can be reconstructed on-board to obtain a very precise estimate of the event energy. These highly sensitive detectors

Further author information: (Send correspondence to Philippe Peille)
E-mail: philippe.peille@cnes.fr

Table 1. The X-IFU top-level performance requirements.

Performance	Requirement
Field of View	5' equivalent diameter
Pixel size	< 5"
Energy range	0.2–12 keV
Quantum efficiency	> 16 % at 0.35 keV
	> 67 % at 1 keV
	> 72 % at 7 keV
	> 50 % at 9.5 keV (TBC)
Energy resolution	2.5 eV (FWHM) at 7 keV
Count rate capability	> 80 % high res events at 0.25 cps/pxl (goal at 1.6)
	> 80 % high res events at 1 mCrab (goal at 10 mCrab) > 50 % 10 eV events at 1 Crab in the 5 – 8 keV band
Non X-ray background	< 5×10^{-3} counts/s/cm ² /keV

will be integrated at the heart of a large cryostat providing, in combination with a complex cryo-chain [6], the cold and clean environment necessary to their operation.

Table 1 summarizes the main X-IFU top-level performance requirements used for the design of the instrument along the phase A. In this article, we present an overview of the current predicted performances of the instrument as well as their modeling. We notably cover the quantum efficiency (Sec. 2), the non-X-ray background level (Sec. 3), the energy resolution (Sec. 4), and the count-rate capability (Sec. 5).

2. QUANTUM EFFICIENCY AND EFFECTIVE AREA

The X-IFU quantum efficiency is determined by four elements of the instrument: the pixels stopping power, the TES matrix filling factor, the thermal filters transmission, and the contamination. Coupled with the mirror area as a function of energy, this quantity defines the total effective area of the instrument.

- The X-ray stopping power will be ensured by absorbers deposited onto the TES thermometers. Their design result from a trade-off between the pixel heat capacity, which drives the pixel resolution and linear range, and its absorption in the scientific band. A solution with a bilayer of 1.7 μm gold and 4.2 μm bismuth has been identified, in which the gold provides the bulk of the heat capacity and a good thermalization layer, and bismuth is added to gain stopping power at a lower heat capacity cost, reaching 90 % at 7 keV. These absorbers will have a size of 245 μm and be separated by gaps of 4 μm corresponding to a size on the sky of 4.3" and a filling factor of $\sim 97\%$ [2].
- Thermal filters will be implemented at five different temperatures from the outer shell, down to the 50mK detection stage, to avoid infrared and optical loading on the sensitive X-IFU pixels. Each filter is made of an aluminum thin film of 30 nm deposited on a 45 nm polyimide substrate. For mechanical support as well as rejection of radio frequency radiation, stainless steel meshes are deposited onto the four outer filters. The 50 mK filter will feature a niobium mesh to avoid disrupting the magnetic field environment of the detectors. Mechanical integrity after launch load vibrations has been demonstrated for meshes with a $\sim 4\%$ blocking factor per filter. Future optimization will aim at reaching $\sim 2\%$ per filter (see more details in [7]). The transmission of the filters is limited at low energies by the minimum thickness of the fabricated aluminum layer as well as the need to reject UV radiation, and by the blocking factor of the meshes at high energy.
- Outgassed materials and water from the platform and the inside of the dewar may be deposited on the various surfaces along the optical path and degrade the quantum efficiency of the instrument. This is

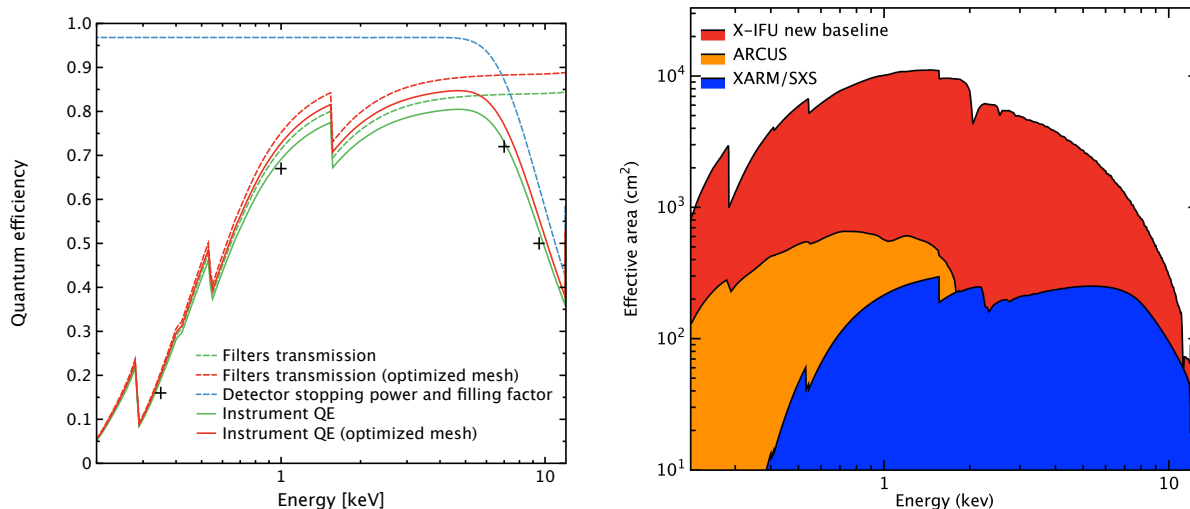


Figure 1. Left: The quantum efficiency of the X-IFU instrument and its contributors (excluding contamination). The performance requirements are indicated with '+'. Right: The X-IFU effective area compared to other high resolution instruments: the next generation grating spectrometer onboard the *Arcus* mission, and the Resolve microcalorimeter onboard the *Xarm* mission.

especially true for the coldest surfaces, which will act as natural condensation traps. A careful design of the aperture cylinder and of the instrument interface as well as an adapted cool-down strategy will aim at limiting this effect. At this stage, we allocate 10% loss of transmission at 0.35 keV and 1% at 1 keV from contamination. This corresponds to a maximum of $\sim 3.2 \mu\text{g}/\text{cm}^2$ of common contamination material. Negligible loss of transmission is expected above 1 keV.

Figure 1 (left) shows the contamination-free quantum efficiency of the instrument as a function of energy with its contributors. With contamination included, a margin of at least 2% is found with the current filter configuration and $> 7\%$ with the optimized mesh design. Figure 1 (right) in turn shows the overall effective area of the instrument, illustrating the leap forward compared to other planned/proposed high resolution missions obtained in combination with the large area *Athena* optics [8,9].

3. NON X-RAY BACKGROUND

High-energy galactic cosmic rays and the secondaries they generate from the instrument structure will sometimes deposit an amount of energy compatible with the X-IFU bandpass. These events, if not properly flagged, will be mixed with the science data and constitute the so-called non X-ray background. In order to limit its level, the X-IFU will feature a cryogenic anticoincidence (cryoAC) detector located ~ 1 mm below the main array [10]. Events happening coincidentally in different locations of the array will also be rejected, as they are most likely created by a shower of secondaries.

The X-IFU background was evaluated in different configurations using Geant4 v.10.2 and the Space Physics List defined in the AREMBES framework and endorsed by ESA (see more details in [11]). To do so, a detailed mass model of the instrument was built using the current X-IFU design. Special care was notably taken to represent the focal plane assembly geometry, from which most of the secondary events originate. In Figure 2 (left), we see the effectiveness of different solutions to reduce the non X-ray background. The cryoAC is clearly determinant in reaching the required performance by rejecting more than 98% of the false events. An optimized passive shield of 20 μm bismuth and 250 μm kapton was further designed to stop part of the secondaries generated in the niobium shield located in the vicinity of the detectors and allows to decrease the background level to $\sim 4.6 \times 10^{-3}$ cts/s/cm²/keV in the 2 to 10 keV band when all cosmic ray contributions are taken into account (see Figure 2). This gives an overall margin of $\sim 10\%$ with respect to the requirement, knowing that all simulations were performed using the worst case galactic cosmic ray spectrum.

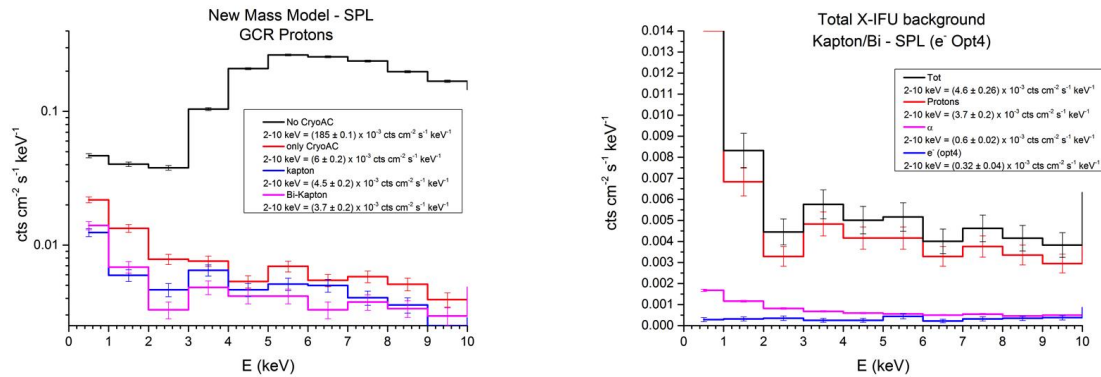


Figure 2. Left: The simulated X-IFU background generated by galactic cosmic ray protons in different configurations: without the CryoAC detector (black line), with the insertion of the CryoAC (red), with a kapton passive shield (blue), and with the optimized kapton/bismuth shield (magenta). Right: Total X-IFU background spectra and integrated values, with all components included (protons, alpha and electrons).

4. ENERGY RESOLUTION

To verify that the instrument design will meet the very challenging 2.5 eV FWHM requirement at 7 keV, it is necessary to build a solid energy resolution budget, taking into account all the effects that will eventually affect the energy measurement. Due to the complexity of the system and the sensitivity of the detectors (which allows to reach this level of performance), these effects actually number in the tens. This effort was initially started, as described in [12], by allocating to each of these contributors the same quadrature degradation of the resolution, apart naturally from the TES detectors that represent the bulk of the resolution with a 2 eV predicted performance and the DACs of the Digital Readout Electronics that were deemed critical from the start of the project and allocated a larger contribution. Since then, these allocations have been modified to match our growing understanding of the different contributors and of their criticality. We now distinguish three levels of contributions adding in quadrature:

- The standard contribution is 0.2 eV, which was essentially derived from the number of items in the budget and the remaining margin between the 2 eV detector performance and the instrument level requirement.
- A smaller contribution of 0.1 eV is allocated to effects deemed less challenging or impacting the X-IFU performance in an indirect manner (e.g. the drift of the SQUID bias current).
- A larger contribution is set apart for items considered challenging or limited by technology, such as the DACs, or the SQUID tandem.

The X-IFU energy resolution budget can also be broken down into three main categories:

- Noise generated by or picked-up from the different elements of the readout chain (see Figure 3 and [4, 5] for more details on the design of the readout chain).
- Low frequency drifts of the environment of the detectors and electronics that change the operating conditions of the instrument and for a large part depend on the sensitivity of the detectors (e.g. fluctuations from the thermal bath).
- Higher order effects that cannot be associated to either category (e.g. crosstalk as described in Sect. 5).

In this section, we will not review the status of each of these individual contributors, some of which warrant individual models and studies, but focus on the ones that are being verified through simulations of the X-IFU pixels and their readout system, which constitute the bulk of the resolution budget. A subsequent publication should address the full energy resolution budget in more details.

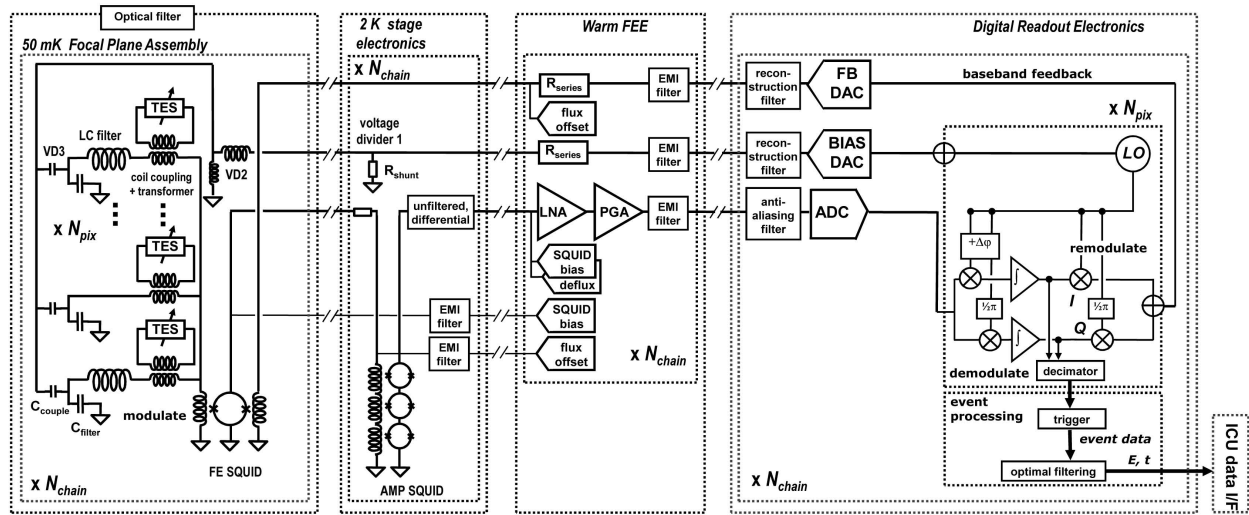


Figure 3. Schematic of the X-IFU FDM readout chain. The biasing of the pixels is provided by DACs creating a frequency comb per readout channel of 40 carriers that get selected in the coldest stage by high quality factor LC filters such that each pixel sees a single carrier. The currents from all pixels in a channel are then summed and read out by a single front-end SQUID and amplified up to the digital readout electronics (DRE). After demodulation, the scientific signal is finally analyzed on board by the Event Processor. The linearization of the first stage SQUID is ensured by a baseband feedback loop controlled by the DRE [3].

4.1 Noise from the TES and readout system

The energy resolution of the TES pixels and their readout system is being evaluated using the `tessim` tool [13]. This simulator performs a numerical integration of the electro-thermal equations of the TES in its first stage readout circuit. For simplicity reasons and in the absence of an AC bias model of the TES, the actual 50 mK readout circuit (see Figure 3) is modeled in that tool by its DC Thevenin equivalent. The non-linearity of the first stage readout, as well as the non-stationary noise from the TES, the thermal bath and the readout electronics is taken into account. In particular, noise from the bias line is simulated as constant voltage noise, whereas noise from the feedback and SQUID output lines are added as white broadband noise sources. Future versions of these simulations will notably aim at having a more representative model of the AC behavior of the system.

To compute the acceptable noise levels in physical units for the different contributors, we simulate sets of 7 keV pulses for different values of amplifier and bias line noise, and reconstruct them with standard current space optimal filtering to estimate the total resolution including all the noise contributions. Figure 4 (left) illustrates the behavior as a function of the amplifier noise for a constant bias line noise level and Table 2 gives the current allocations for the different noise sources derived from this exercise. One notices that for an equal level of noise in the bias and amplifier lines, the former has a much smaller effect on the resolution than the latter. This is due to the fact that noise from the bias line is bandwidth limited by the TES whereas amplifier line noise acts as a broadband contributor. Reallocations were made such that the noise values in physical units are the same in both lines for the two DACs, cable noise and susceptibility noise. The shunt resistor allocation was chosen as a compromise between its noise and its heat load on the 2K stage.

4.2 Pixel sensitivity and influence of the environment

The `tessim` tool also allows to predict the sensitivity of the readout chain response to variations in the pixels environment. Sensitivity values of $-120 \text{ meV}/\mu\text{K}$ to the pixel bath temperature and $-13 \text{ meV}/\text{ppm}$ to the bias voltage were found at 7 keV, with a close to linear scaling as a function of energy. We note that the bath temperature sensitivity is consistent with the highest measured values obtained on similar pixels [2]. These

Table 2. The X-IFU readout chain noise budget.

Contributor	Noise level	Allocation
TES pixel	–	2.0 eV
Total readout noise referred to the SQUID input	4.6 pA/$\sqrt{\text{Hz}}$	0.94 eV
Feedback DAC	3.7 pA/ $\sqrt{\text{Hz}}$	0.7 eV
SQUID tandem	2.1 pA/ $\sqrt{\text{Hz}}$	0.4 eV
LNA	1.1 pA/ $\sqrt{\text{Hz}}$	0.2 eV
ADC	1.1 pA/ $\sqrt{\text{Hz}}$	0.2 eV
Cable noise	0.55 pA/ $\sqrt{\text{Hz}}$	0.1 eV
Conducted susceptibility	0.55 pA/ $\sqrt{\text{Hz}}$	0.1 eV
Total bias current noise referred to the SQUID input	4.3 pA/$\sqrt{\text{Hz}}$	0.3 eV
AC bias DAC	3.7 pA/ $\sqrt{\text{Hz}}$	0.25 eV
Shunt resistor	2.1 pA/ $\sqrt{\text{Hz}}$	0.15 eV
Conducted susceptibility	0.55 pA/ $\sqrt{\text{Hz}}$	0.04 eV
Cable noise	0.55 pA/ $\sqrt{\text{Hz}}$	0.04 eV
Total energy resolution at readout chain level	–	2.23 eV

values can then be used to derive the resolution degradation from the 0.9 μK rms stability of the 50 mK stage [6] (0.26 eV at 7 keV) and the 17 ppm* stability on 1000 s time scale[†] of the bias DAC (0.1 eV at 7 keV). The other fiducial allocations depending on the pixel sensitivity to its thermal bath (the effect of cosmic ray hits on the detector wafer and FPA structure, as well as the degradation from microvibrations) can also be adjusted as a function of energy using the scaling found in simulations. From this, we obtain the instrument resolution including the readout system and the pixel sensitivity as a function of energy (see green curve in Figure 4, right).

4.3 Instrument level energy resolution

After adding the quadrature sum of the rest of the allocations (0.97 eV) to the contributions described in the previous subsections, we obtain the energy resolution curve as a function of energy shown in Figure 4 (right). The full instrument resolution amounts to ~ 2.45 eV at 7 keV, leaving a margin of ~ 0.5 eV with respect to the 2.5 eV requirement. For comparison, this margin is larger than the full allocation of the SQUID tandem (see Table 2). We further note that better performances are typically predicted at lower energies (~ 2.2 eV at 1 keV), which is of particular interest to science cases requiring the best possible resolution at low energy (e.g. the detection of weak WHIM absorption lines from GRB afterglows whose detectability scales with the inverse of the square of the resolution [15]).

5. COUNT RATE CAPABILITY

During the observation of the brightest X-ray sources, the X-IFU will receive photon rates going up to tens of counts per second (cps) per pixel and hundreds per readout channel. In this regime, usually negligible effects like event processing limitations and crosstalk will start to dominate. In this section, we present how these effects are being estimated and eventually incorporated into the instrument end-to-end simulator to assess the performance of the X-IFU as a function of count rate. This work mainly builds on the setup presented in [16], where more details can be found. We nonetheless recall here the main elements of these simulations. We further note that this previous study has been conducted with the so-called *as proposed* mirror configuration (20 mirror rows for

*Assuming a constant drift across a calibration period, a linear gain drift of 17 ppm will induce an 0.1 eV FWHM broadening at 7 keV. This is what is allocated to the feedback DAC stability which acts as such a linear scaling. The DAC bias is then assumed to have the same stability.

[†]Longer term gain drifts will be corrected through the use of the MXS [14].

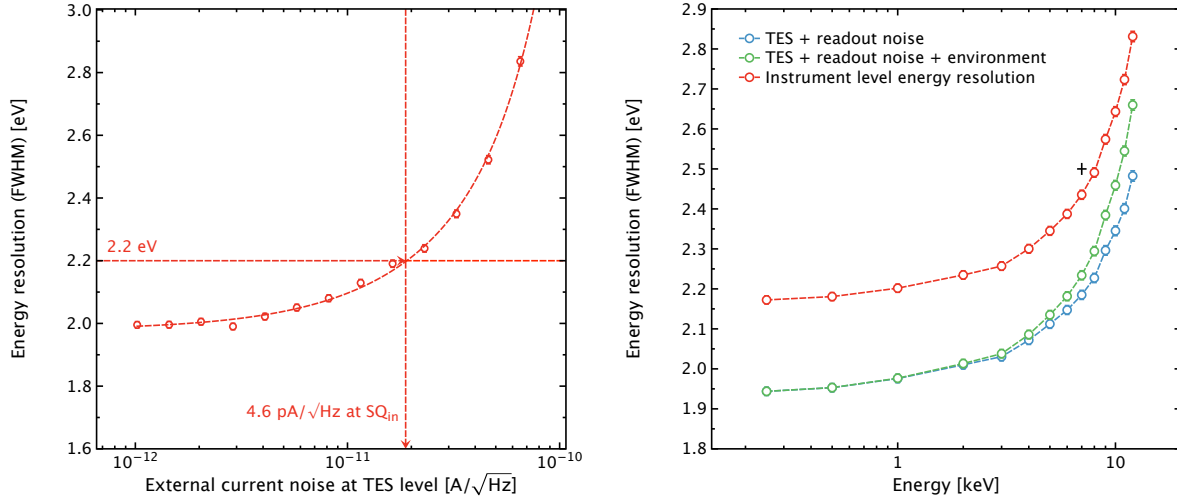


Figure 4. Left: Energy resolution degradation as a function of the amplifier noise level. The vertical line indicates the noise allocated to the X-IFU readout electronics. Right: Estimated energy resolution as a function of energy. The ‘+’ sign indicates the 7 keV requirement (2.5 eV). The error bars indicate in both figures the 1σ statistical error of the simulations.

an effective area of 2 m^2 at 1 keV), which has now been replaced by a smaller new mirror configuration with 15 mirror rows ($\sim 1.4\text{ m}^2$ at 1 keV) [9].

5.1 Event processing limitations

At high count rates, the X-ray pulses in the pixels timelines start to get packed. This limits the performance of the on-board reconstruction by essentially two effects: when a photon arrives too close to a preceding event, its measured energy will be biased by the signal leaked from the previous pulse. Such events are called secondaries and need to be rejected from the science data. A too close subsequent pulse will prevent the use of the longest, highest resolution optimal filter and therefore degrade the resolution of the event. Different event grades can thus be defined as a function of pulse separation to characterize this effect on board [17].

For this study, we consider secondary events separated by less than 10 pixel time constants (at critical damping – as they are planned to be operated) from their preceding pulse as invalid. For the other valid events, the energy resolution as a function of the available record length is given by: $\Delta E(t_{\text{rec}}) = \frac{\lim_{t_{\text{rec}} \rightarrow \infty} \Delta E}{\sqrt{1 - 1/(2t_{\text{rec}}f_{\text{eff}})}} [18]$.

In practice, different secondaries grades should exist at closer pulse separations as some of these events will be suitable for lower resolution spectroscopy (see e.g. [19]). For the purpose of estimating the count rate capability of the instrument, we however prefer to consider them all as invalid, as it remains unclear for now how they would be calibrated over the full energy bandpass of the instrument. The different event grades are summarized in Table 3. The filter lengths of the valid grades were rounded up to the highest power of two to match an optimized processing efficiency.

5.2 Crosstalk

Crosstalk happens when scientific signal from a photon impact (perpetrator) leaks into another pixel and modifies the energy measurement of an other (victim) event in that second pixel. While almost negligible at low count rates, its effect will grow steadily with the fraction of overlapping events. For the moment, two main types of crosstalk mechanisms are foreseen for the X-IFU instrument and have been implemented in the end-to-end simulator[‡]:

[‡]Crosstalk due to the non-linearity of the readout chain was also studied in [16] and found to be of second order with respect to the other two mechanisms.

Table 3. Definition of the different event grades, with a sampling rate of 156.25 kHz.

Grade	Time since previous pulse	Time until next pulse	Filter length	Energy resolution
High res.	≥ 2.9 ms	≥ 52 ms	8192 samples	2.5 eV
Medium res.	≥ 2.9 ms	≥ 3.3 ms	512 samples	3 eV
Limited res.	≥ 2.9 ms	≥ 1.6 ms	256 samples	7 eV
Low res.	≥ 2.9 ms	-	4 samples	~ 30 eV

- Thermal crosstalk originating from the thermal coupling between adjacent pixels. We modeled this effect by an energy transfer from the perpetrator to the victim pixel and took as a conservative estimate the levels measured by [20] in a faster 8x8 pixels array: 10^{-3} for the first neighbor, 4×10^{-4} for diagonal neighbors, and 8×10^{-5} for second neighbors. The final effect on the victim event after optimal filtering as a function of the time phasing of the events was characterized with the `tessim` tool by simulating the impact of a 1 eV leakage onto a 7 keV victim impact as a function of time separation. We then assumed a linear dependency as a function of the equivalent crosstalk energy.
- Electrical crosstalk created by the FDM first stage readout circuit. This process was studied using `tessim` and characterized as a function of the frequencies of the pixels involved and the time separation of the events (see more details in [16, 21]). Two main components were identified: carrier overlap (a direct leakage signal due to the limited quality factor of the LC filters) and common impedance crosstalk (the slower thermal reaction of the victim pixel to the changed current in the perpetrator pixel through the common impedance in the first stage circuit – mostly the SQUID input coil, see Figure 3).

5.3 X-IFU performance as a function of count rate

With the different degradations characterized, we can now estimate the performance of the instrument as a function of count rate. This was conducted using the `xifupipeline` tool of the SIXTE software suite [22]: following a Monte Carlo process, this simulator generates photons from a catalog of X-ray sources and follows them through the imaging and detection processes. The *Athena* telescope in combination with the X-IFU filters are modeled through a set of calibration files (ARF, PSF, and vignetting) allowing to create the proper spatial and timing distribution of the photon impacts onto the focal plane. In particular, this setup allows to simulate the effect of mirror defocusing, which eases the observation of the brightest sources: the *Athena* mirror is planned to be integrated on an hexapod platform that allows to put the mirror up to 35 mm away from its focused position and spread the PSF over several hundreds of pixels (see e.g. [1]). A geometrical model of the X-IFU detector array then affects the events to the relevant pixels and readout channels. Finally, the readout energy of each event is obtained randomly from a response matrix corresponding to its grade (see Sect. 5.1) while taking into account the energy offset generated by potential crosstalk events through coupling matrices (see Sect. 5.2).

Figure 5 shows the results of the end-to-end simulation of the three sizing science cases for the X-IFU count rate capability:

- The high resolution observation of a bright extended source, typically the center of a bright cluster like Perseus. This was modeled as a flat field with an absorbed 5 keV thermal spectrum.
- The high resolution observation of a bright point source with a defocus length of 35 mm. The point source was modeled with the same spectral distribution as the Crab, i.e. an absorbed power law. The main science case requiring high resolution at these count rates is the detection of WHIM absorption lines in the spectrum of gamma-ray bursts afterglows.
- The observation of a very bright point source (up to 1 Crab) with a defocus length of 35 mm, the use of a 100 μm -thick beryllium filter to cut most of the numerous < 3 keV photons, and degraded resolution (10 eV). Here too we took the spectral distribution of the Crab even if the main targets at these count rates would be galactic binaries to detect strongly blue-shifted iron lines in the 5 to 8 keV range generated

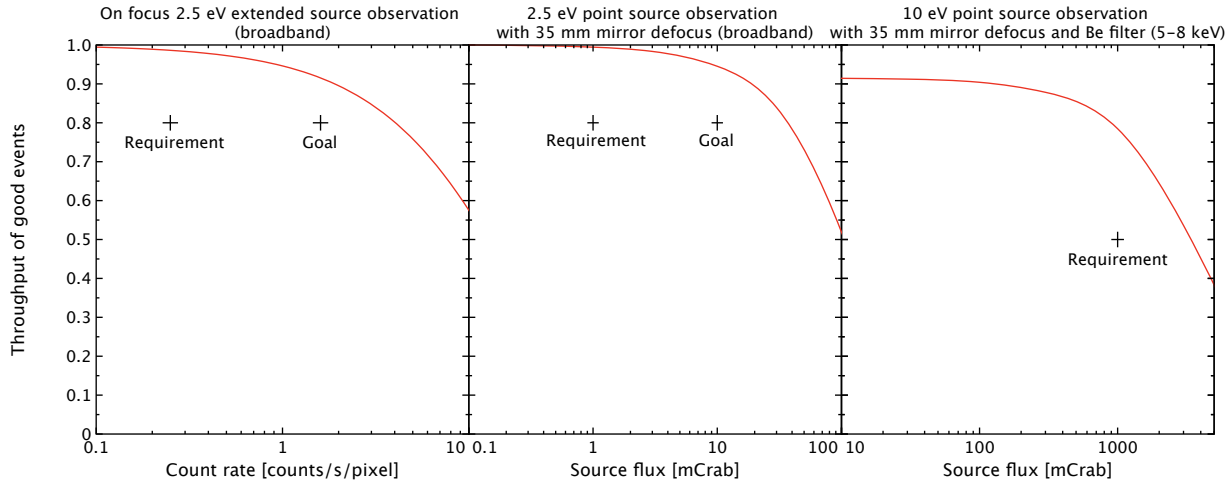


Figure 5. Throughput of good events for the three sizing science cases for the X-IFU count rate capability. Left: High resolution observation of an extended source with a thermal spectrum. Middle: High resolution observation of a bright defocussed Crab-like point source. 10 mCrab corresponds to a count rate of ~ 650 cps over the array with $\gtrsim 600$ pixels receiving more than 0.6 cps for a maximum of 1.2 cps. Right: 10 eV observation of the same source but with a beryllium filter cutting most of the low energy events. 1 Crab corresponds to ~ 93000 cps over the full matrix with a maximum count rate of $\gtrsim 30$ cps and $\gtrsim 200$ pixels receiving more than 15 cps. In all figures, the '+' signs indicate the X-IFU count rate requirements and goals.

by black hole winds. These sources actually feature much thicker column densities than the Crab. An optimization of the beryllium filter thickness should be done eventually to limit the loss of low energy photons while keeping the required count rate capability.

For simplicity, in these figures, the effect of crosstalk is accounted for as throughput loss: an event is considered as high resolution if it has the appropriate grade and has been influenced by crosstalk by less than 0.2 eV (the crosstalk allocation in the energy resolution budget). A valid 10 eV resolution event in turn corresponds to an original limited resolution event (7 eV) with less than 4 eV crosstalk influence. We note that this assumes an a priori knowledge of the crosstalk effect, which is deterministic, but no post correction.

Overall, we see that all count rate requirements and goals are met with a significant margin of at least a factor of two in count rate.

6. CONCLUSION

We have presented here an overview of the predicted performances of the X-IFU at the approach of the end of the phase A study. Consolidated budgets and simulations have been developed, showing that the main performance requirements should be met with appropriate margins. In particular, we have shown that the X-IFU shall exceed its specified (even goal) count rate by more than a factor of two. This margin may be spent in the future to accommodate slower, easier to read out pixels and draw additional margin for the energy resolution budget. Alternatively, an increase of the pixel size to diminish the number of readout channels could reduce the thermal loads in the cold stages and the overall instrument mass budget.

REFERENCES

- [1] Barret, D., Lam Trong, T., den Herder, J.-W., Piro, L., Barcons, X., Huovelin, J., Kelley, R., Mas-Hesse, J. M., Mitsuda, K., Paltani, S., Rauw, G., Rozanska, A., Wilms, J., Barbera, M., Bozzo, E., Ceballos, M. T., Charles, I., Decourchelle, A., den Hartog, R., Duval, J.-M., Fiore, F., Gatti, F., Goldwurm, A., Jackson, B., Jonker, P., Kilbourne, C., Macculi, C., Mendez, M., Molendi, S., Orleanski, P., Pajot, F., Pointecouteau, E., Porter, F., Pratt, G. W., Prêle, D., Ravera, L., Renotte, E., Schaye, J., Shinozaki, K., Valenziano, L., Vink, J., Webb, N., and Yamasaki, N. Y., “The Athena X-ray Integral Field Unit (X-IFU),” *Proc. SPIE* **9905**, 9905–83 (July 2016).
- [2] Smith, S. J., Adams, J. S., Bandler, S. R., Betancourt-Martinez, J. L., Chervenak, J. A., Chiao, M., Datesman, A. M., Eckart, M. E., Ewin, A. J., Finkbeiner, F. M., Kelley, R. L., Kilbourne, C. A., Porter, F. S., Sadleir, J. E., Wassel, E. J., Yoon, W., Bennett, D. A., Doriese, W. B., Hilton, G. C., Swetz, D. S., Ullom, J. N., Akamatsu, H., Gottardi, L., den Hartog, R. H., Jackson, B. D., van der Kuur, J., Barret, D., and Peille, P., “TES pixel parameter design of the microcalorimeter array for the x-ray integral field unit on ATHENA,” *Proc. SPIE* **9905**, 9905–85 (July 2016).
- [3] Ravera, L., Cara, C., Ceballos, M. T., Barcons, X., Barret, D., Clédassou, R., Clénet, A., Cobo, B., Doumayrou, E., den Hartog, R. H., van Leeuwen, B.-J., van Loon, D., Mas-Hesse, J. M., Pigot, C., and Pointecouteau, E., “The DRE: the digital readout electronics for ATHENA X-IFU,” *Proc. SPIE* **9144**, 91445T (July 2014).
- [4] Akamatsu, H., Gottardi, L., van der Kuur, J., de Vries, C. P., Ravensberg, K., Adams, J. S., Bandler, S. R., Bruijn, M. P., Chervenak, J. A., Kilbourne, C. A., Kiviranta, M., van der Linden, A. J., Jackson, B. D., and Smith, S. J., “Development of frequency domain multiplexing for the X-ray Integral Field unit (X-IFU) on the Athena,” *Proc. SPIE* **9905**, 99055S (July 2016).
- [5] Akamatsu, H., Gottardi, L., van der Kuur, J., de Vries, C. P., Bruijn, M. P., and et al, “Development of frequency domain multiplexing for the X-ray Integral Field Unit (X-IFU),” in [*Space Telescopes and Instrumentation 2018: Ultraviolet to Gamma Ray*], *Proc. SPIE* **10699**, 10699–58 (July 2018).
- [6] Charles, I., Daniel, C., André, J., Duband, L., Duval, J.-M., den Hartog, R. H., Mitsuda, K., Shinozaki, K., van Weers, H. J., and Yamasaki, N. Y., “Preliminary thermal architecture of the X-IFU instrument dewar,” in [*Space Telescopes and Instrumentation 2016: Ultraviolet to Gamma Ray*], *Proc. SPIE* **9905**, 9905–87 (July 2016).
- [7] Barbera, M. and et al, “Status of the ATHENA X-IFU thermal filters development at the end of the phase A,” in [*Space Telescopes and Instrumentation 2018: Ultraviolet to Gamma Ray: Ultraviolet to Gamma Ray*], *Proc. SPIE* **10699**, 10699–62 (July 2018).
- [8] Bavdaz, M., Wille, E., Shortt, B., Fransen, S., Collon, M., Barriere, N., Yanson, A., Vacanti, G., Haneveld, J., van Baren, C., Zuknik, K.-H., Christensen, F., Della Monica Ferreira, D., Krumrey, M., Burwitz, V., Pareschi, G., Spiga, D., Valsecchi, G., and Vernani, D., “The ATHENA optics development,” in [*Space Telescopes and Instrumentation 2016: Ultraviolet to Gamma Ray*], *Proc. SPIE* **9905**, 990527 (July 2016).
- [9] Bavdaz, M., Wille, E., Ayre, M., Ferreira, I., Shortt, B., Fransen, S., and et al, “Development of the ATHENA mirror,” in [*Space Telescopes and Instrumentation 2018: Ultraviolet to Gamma Ray: Ultraviolet to Gamma Ray*], *Proc. SPIE* **10699**, 10699–32 (July 2018).
- [10] D’Andrea, M., Argan, A., Lotti, S., Macculi, C., Piro, L., Biasotti, M., Corsini, D., Gatti, F., and Torrioli, G., “The Cryogenic Anti-Coincidence detector for ATHENA X-IFU: pulse analysis of the AC-S7 single pixel prototype,” in [*Space Telescopes and Instrumentation 2016: Ultraviolet to Gamma Ray*], *Proc. SPIE* **9905**, 99055X (July 2016).
- [11] Lotti, S. and et al, “Estimates for the background of the ATHENA X-IFU instrument: the Cosmic Rays contribution,” in [*Space Telescopes and Instrumentation 2018: Ultraviolet to Gamma Ray*], *Proc. SPIE* **10699**, 10699–61 (July 2018).
- [12] den Hartog, R., Barret, D., Gottardi, L., den Herder, J.-W., Jackson, B., de Korte, P., van der Kuur, J., van Leeuwen, B.-J., van Loon, D., Nieuwenhuizen, A., and Ravera, L., “Requirements for the detectors and read-out of ATHENA X-IFU,” in [*Space Telescopes and Instrumentation 2014: Ultraviolet to Gamma Ray*], *Proc. SPIE* **9144**, 91445Q (July 2014).

- [13] Wilms, J., Smith, S. J., Peille, P., Ceballos, M. T., Cobo, B., Dauser, T., Brand, T., den Hartog, R., Bandler, S. R., de Plaa, J., and den Herder, J.-W., “TESSIM: a simulator for the ATHENA X-IFU,” *Proc. SPIE* **9905**, 9905–192 (July 2016).
- [14] de Vries, C. P., den Herder, J. W., Costantini, E., Aarts, H., Lowes, P., Kaastra, J. S., Kelley, R., Gendreau, K., Arzoumanian, Z., Koenecke, R., Haas, D., Paltani, S., Mitsuda, K., and Yamasaki, N. Y., “Filters and calibration sources for the soft x-ray spectrometer (SXS) instrument on ASTRO-H,” in [*Space Telescopes and Instrumentation 2010: Ultraviolet to Gamma Ray*], *Proc. SPIE* **7732**, 773213 (July 2010).
- [15] Kaastra, J., Finoguenov, A., Nicastro, F., Branchini, E., Schaye, J., Cappelluti, N., Nevalainen, J., Barcons, X., Bregman, J., Croston, J., Dolag, K., Etti, S., Galeazzi, M., Ohashi, T., Piro, L., Pointecouteau, E., Pratt, G., Reiprich, T., Roncarelli, M., Sanders, J., Takei, Y., and Ursino, E., “The Hot and Energetic Universe: The missing baryons and the warm-hot intergalactic medium,” *ArXiv e-prints* (June 2013).
- [16] Peille, P., Dauser, T., Kirsch, C., den Hartog, R., Cucchetti, E., Wilms, J., Barret, D., den Herder, J.-W., and Piro, L., “The performance of the athena x-ray integral field unit at very high count rates,” *Journal of Low Temperature Physics* (May 2018).
- [17] Seta, H., Tashiro, M. S., Ishisaki, Y., Tsujimoto, M., Shimoda, Y., Abe, Y., Yasuda, T., Takeda, S., Asahina, M., Hiyama, Y., Yamaguchi, S., Terada, Y., Boyce, K. R., Porter, F. S., Kilbourne, C. A., Kelley, R. L., Fujimoto, R., Takei, Y., Mitsuda, K., Matsuda, K., and Masukawa, K., “The Digital Processing System for the Soft X-Ray Spectrometer Onboard ASTRO-H – The Design and the Performance –,” *IEEE Transactions on Nuclear Science* **59**, 366–372 (Apr. 2012).
- [18] Doriese, W. B., Adams, J. S., Hilton, G. C., Irwin, K. D., Kilbourne, C. A., Schima, F. J., and Ullom, J. N., “Optimal filtering, record length, and count rate in transition-edge-sensor microcalorimeters,” *American Institute of Physics Conference Series* **1185**, 450–453 (Dec. 2009).
- [19] Lee, S. J., Bandler, S. R., Busch, S. E., Adams, J. S., Chervenak, J. A., Eckart, M. E., Ewin, A. J., Finkbeiner, F. M., Kelley, R. L., Kilbourne, C. A., Porst, J.-P., Porter, F. S., Sadleir, J. E., Smith, S. J., and Wassel, E. J., “High Count-Rate Studies of Small-Pitch Transition-Edge Sensor X-ray Microcalorimeters,” *Journal of Low Temperature Physics* **176**, 597–603 (Aug. 2014).
- [20] Iyomoto, N., Bandler, S. R., Brekosky, R. P., Brown, A.-D., Chervenak, J. A., Figueroa-Feliciano, E., Finkbeiner, F. M., Kelley, R. L., Kilbourne, C. A., Porter, F. S., Sadleir, J. E., and Smith, S. J., “Heat Sinking and Crosstalk for Large, Close-Packed Arrays of Microcalorimeters,” *Journal of Low Temperature Physics* **151**, 506–512 (Apr. 2008).
- [21] den Hartog, R., Kirsch, C., de Vries, C., Akamatsu, H., Dauser, T., Peille, P., Cucchetti, E., Jackson, B., Bandler, S., Smith, S., and Wilms, J., “Crosstalk in an FDM Laboratory Setup and the Athena X-IFU End-to-End Simulator,” *Journal of Low Temperature Physics* (Apr. 2018).
- [22] Wilms, J., Brand, T., Barret, D., Beuchert, T., den Herder, J.-W., Kreykenbohm, I., Lotti, S., Meidinger, N., Nandra, K., Peille, P., Piro, L., Rau, A., Schmid, C., Smith, R. K., Tenzer, C., Wille, M., and Willingale, R., “ATHENA end-to-end simulations,” *Proc. SPIE* **9144**, 91445X (July 2014).